sustainability

MDPI

Article

Optimization of Pyrolysis Kinetics and Blending Ratio of *Salix psammophila* and Corn Stover Under a Nitrogen Atmosphere Based on TG-DTG and SEM

Zhen Li, Hongyu Fu *, Jinlu Yu, Hongqiang Wang, Wenkai Wang and Chao Fan

Faculty of Mechanical Engineering, Inner Mongolia University of Science and Technology, Baotou 014010, China; lizhen_730106@126.com (Z.L.); yjl20010615@163.com (J.Y.); hunter_930321@163.com (H.W.); wwk200102@163.com (W.W.); fc20011022@163.com (C.F.)

* Correspondence: fuhongyu0823@163.com

Abstract

Understanding the thermal decomposition behavior and kinetic characteristics of blended biomass is crucial for optimizing thermochemical conversion processes. This study systematically investigates the synergistic pyrolysis (thermal decomposition) behavior of *Salix psammophila* (SP) and corn stover (CS) under a nitrogen atmosphere, with particular emphasis on process behavior and reaction kinetics (and thermodynamic feasibility). Based on elemental and proximate analyses, SP provides high calorific value and lignin content, while CS contributes high volatile matter and cellulose, enabling complementary interaction during thermal conversion. Three blending ratios (CS:SP = 2:1, 3:1, and 5:2) were analyzed using scanning electron microscopy (SEM), Fourier-transform infrared spectroscopy (FTIR), thermogravimetric analysis (TGA), and kinetic evaluation via the Coats–Redfern, Flynn–Wall–Ozawa (FWO), and Kissinger–Akahira–Sunose (KAS) methods, together with thermodynamic parameter estimation (ΔH, ΔS, and ΔG). The results indicate that the 3:1 blend forms an optimized "continuous phase–dispersed phase" structure with an interfacial transition layer of 11–15 μm and uniformly distributed fine pores, promoting effective heat and mass transfer and facilitating volatile-release pathways across the blend interface. At a heating rate of 15 °C·min^{-1}, this blend exhibits the lowest onset temperature of rapid mass loss (T_{onset}, 209 °C), the highest comprehensive pyrolysis performance index (S_N, 3.01), and stable DTG profiles. Kinetic analysis confirmed that the 3:1 blend exhibits the lowest activation energy during the devolatilization stage, indicating enhanced reaction feasibility under inert conditions. The results provide mechanistic insight into biomass blending effects and offer guidance for process optimization in inert-atmosphere thermochemical conversion systems.

Keywords: blended biomass; thermogravimetric analysis; pyrolysis characteristics; renewable energy; kinetic analysis; SEM microstructure

Check for updates

Academic Editors: Konstantinos G. Kalogiannis and Maria Antoniadou

Received: 20 January 2026
Revised: 25 February 2026
Accepted: 2 March 2026
Published: 5 March 2026

Copyright: © 2026 by the authors. Licensee MDPI, Basel, Switzerland. This article is an open access article distributed under the terms and conditions of the Creative Commons Attribution (CC BY) license.

1. Introduction

Biomass accounts for approximately 14% of global energy demand, ranking as the world's fourth largest energy source. As typical biomass resources, *Salix psammophila* and corn stover constitute significant energy reserves for developing countries, meeting about 35% of their energy needs [1,2]. Under carbon neutrality goals, biomass energy holds irreplaceable strategic significance for substituting fossil fuels and reducing greenhouse gas emissions. However, open-air burning of corn stover readily leads to surges in pollutants,

such as nitrogen oxides (NO_x) and carbon monoxide (CO), imposing severe environmental burdens [3,4]. Achieving clean and efficient biomass utilization through thermochemical conversion technologies (e.g., pyrolysis, gasification, and staged conversion processes) represents a key pathway for renewable energy development and a core solution to alleviate energy shortages in developing countries [5,6].

Existing biomass co-combustion research [7] predominantly focuses on air atmospheres. Ahmed, I et al. [8] conducted binary mixture experiments of corn stover and wood chips in air, revealing a 15% improvement in the comprehensive combustion index of the blended fuel, confirming the synergistic effects of blending ratios on combustion performance. Li Shan et al. [9] elucidated the dynamic coupling mechanism between volatile release and fixed carbon oxidation through single-particle combustion numerical simulation, laying the foundation for combustion process simulation. However, single-biomass combustion exhibits inherent limitations: corn stover's fine-particle structure predisposes it to coking [10]. While adjusting the air coefficient can reduce coking rates [11], this approach fails to address the fundamental issue of high moisture content in the fuel. Al-Abedi et al. [12,13] innovatively explored the co-combustion of corn stover with municipal solid waste, achieving both reduced NO_x emissions and waste resource utilization, highlighting the environmental potential of mixed fuels. Notably, a mechanistic and kinetic understanding of biomass pyrolysis/thermal conversion under inert N_2 atmospheres remains limited, especially for blended lignocellulosic systems, which hinders the design of N_2-based thermochemical conversion processes.

Based on elemental and industrial analysis [13], the complementary properties of *Salix psammophila* (high calorific value, high lignin) and corn stover (high volatile matter, high cellulose) are significant. This study employs an N_2 atmosphere to investigate the influence of mixing ratios on the microstructure, pyrolysis characteristics, and kinetic parameters of the blended fuel. Through SEM microstructural characterization, TGA pyrolysis testing, and multi-method kinetic analysis, we reveal the regulatory mechanisms governing these properties [14,15]. This establishes a quantitative relationship between blending ratios and pyrolysis efficiency, providing theoretical support for the industrial design of *Salix psammophila*–corn stover blended fuels.

The novel contributions of this study are as follows. Although TGA-based studies on blended biomass are abundant, quantitative links between the blend-interface microstructure and TG-DTG kinetics under a strictly inert N_2 atmosphere remain limited. The novelty of this work lies in: (i) quantifying SEM cross-sectional features (interfacial transition-layer thickness and pore connectivity/uniformity) and linking them to TG-DTG characteristic temperatures and kinetic parameters; (ii) establishing an N_2-based ratio-optimization framework using a consistently defined pyrolysis performance index (SN) together with multi-method kinetic verification (Coats–Redfern, FWO, and KAS); and (iii) providing practical design guidance for *Salix psammophila*–corn stover blends in N_2-atmosphere thermochemical conversion (pyrolysis/gasification pre-treatment).

2. Materials and Methods

2.1. Sample Selection

The experimental materials selected were corn stover and *Salix psammophila*, both widely distributed in Inner Mongolia, China. Their elemental and industrial analysis results are shown in Table 1.

Table 1. Characteristics of experimental samples.

Sample		(CS)	(SP)
Elemental Analysis (%)	C	46.3	52.19
	H	5.6	6.43
	O	47.43	40.91
	N	0.57	0.31
	S	0.1	0.14
Industrial analysis (%)	M_{ad}	1.27	0.72
	A_{ad}	4.02	6.78
	V_{ad}	73.85	76.68
	FC_{ad}	20.86	15.82
Cellulose (%)		40.4970	39.6523
Hemicellulose (%)		19.4433	20.4347
Lignin (%)		12.4294	25.2147
Heating value (MJ kg^{-1})	LHV	16.01	17.31
	HHV	18.61	19.28

Salix psammophila contained 52.19% carbon (C) and 6.43% hydrogen (H), with a higher heating value (HHV) of 19.28 MJ/kg and high lignin content; corn stover exhibited a volatile matter content of 73.85%, a fixed carbon content of 20.86%, and low ash content (4.02%). The complementary nature of these key indicators—calorific value, volatile matter, and ash content—between the two fuels provides the theoretical basis for synergistic co-processing during nitrogen-atmosphere thermochemical conversion [16].

2.2. Design of Mixture Sample Ratios

Three mixed-mass ratios (corn stover: *Salix psammophila*) were set up in the experiment, with pure corn stover and pure *Salix psammophila* serving as controls. Figure 1 shows five types of compressed biomass fuels. The three mixed-mass ratios are as follows:

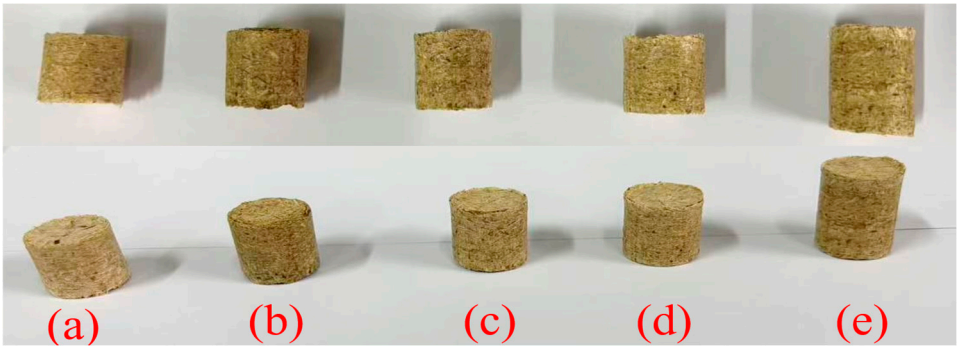


Figure 1. Five types of molded biomass fuel samples: (**a**) corn stover; (**b**) *Salix psammophila*; (**c**) A1 (2:1); (**d**) A2 (3:1); and (**e**) (5:2).

A1 (2:1): High corn stover ratio, aiming to maximize its high volatile matter content for rapid onset of rapid mass loss while verifying *Salix psammophila*'s improvement effect on coking issues;

A2 (3:1): Medium ratio, predicted based on preliminary exploratory experiments and literature insights to balance volatile release rate, pyrolysis stability, and molding properties, representing a potential synergistic optimal blend;

A3 (5:2): Near-equivalent mixing ratio, used to investigate interaction mechanisms when component contents are comparable. All samples had an initial moisture content of 14% (received basis).

2.3. Sample Preparation

Cleaning and Crushing: The raw material surface was rinsed with deionized water to remove external inorganic contaminants (soil, sand, and dust) introduced during collection and storage. This step did not remove intrinsic mineral matter (ash-forming species) in the biomass; instead, it improved experimental reproducibility and mimicked the basic pre-cleaning commonly adopted before densification/thermochemical conversion in practice. After draining, a high-speed multi-function pulverizer was used to crush the material. No chemical demineralization (e.g., acid-washing) was performed; therefore, the intrinsic ash-forming minerals were retained;

Drying: The crushed samples were placed in an electric hot-air constant-temperature drying oven and dried at 105 ± 5 °C for 24 h to obtain absolutely dry samples, ensuring complete moisture removal;

Grinding and Sieving: The dried samples were ground into powder and sieved using standard sieves to achieve a particle size of 18 mesh; as shown in Figure 2 This ensured particle uniformity and minimized experimental errors caused by variations in heat transfer and mass transfer during thermogravimetric analysis;

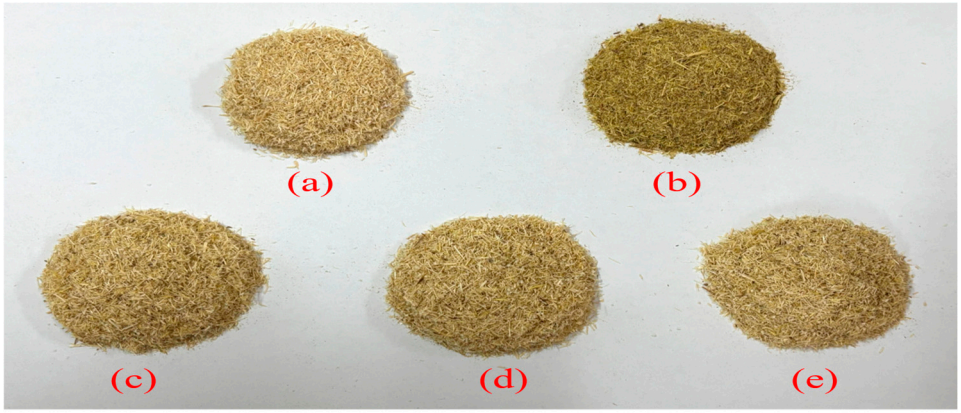


Figure 2. Processed experimental fuel powder particles: (**a**) corn stover; (**b**) *Salix psammophila*; (**c**) A1 (2:1); (**d**) A2 (3:1); and (**e**) (5:2).

Blending and Storage: The corn stover powder and *Salix psammophila* powder were accurately weighed according to the design ratio and mixed in a blending machine for 30 min to ensure uniformity. The prepared blended sample was immediately stored in sealed bags for future use.

2.4. Thermogravimetric Analysis (TGA)

The TGA experiments were conducted using a STA449F3 Jupiter Synchronous Thermal Analyzer from Netzsch, Germany, under the following conditions: sample mass: approximately 10 mg; temperature range: 30–900 °C (ensuring complete sample reaction); heating rates: 5 °C/min, 10 °C/min, 15 °C/min (balancing mechanism analysis and engineering parameter calibration); and carrier gas: high-purity N_2 (99.99%), flow rate 20 mL/min (as protective atmosphere). Each sample was tested in triplicate, with averages taken to ensure data reliability. The DTG peak temperature standard deviation was controlled to within ±2.5 °C/min and TG weight loss deviation to ≤±1.5%.

Terminology in N_2 Environment: In a high-purity nitrogen atmosphere, no external oxidizing agents are present; therefore, the measured mass loss corresponds to thermal decomposition (pyrolysis) and associated volatilization/coke formation. The historical terminology used in thermogravimetric analysis indices (e.g., "rapid mass loss onset/major mass loss endpoint") serves here solely as standardized comparative descriptors for the

initiation and completion of major mass loss, not as characterizations of oxidative processes. The CO/CO_2 observed in inert TGA primarily originates from the decomposition of oxygen-containing functional groups within biomass (endogenous oxygen), not from oxidative combustion reactions.

The following three kinetic methods were employed to calculate the activation energy (E) and pre-exponential factor (A) during thermal decomposition, ensuring the reliability of the results:

1. Coats–Redfern integration method: based on non-isothermal thermodynamic equation integration, kinetic parameters were fitted using the linear relationship between $ln\left|\frac{ln(1-\alpha)}{T^2}\right|$ and 1/T, where α represents the conversion rate;

2. FWO Method: a model-free approach based on the relationship between lnβ and 1/T at constant conversion rate (α), calculating activation energy by fitting the slope of the linear line (β represents heating rate);

3. KAS Method: another model-free approach utilizing the linear relationship between $\ln\left(\frac{\beta}{T_\alpha^2}\right)$ and 1/T at constant α to determine activation energy.

For clarity, the kinetic fitting relations used were: Coats–Redfern: $\ln[g(\alpha)/T^2] = \ln(AR/\beta E) - E/RT$; FWO: $\ln\beta = \ln(AE/Rg(\alpha)) - 5.331 - 1.052(E/RT)$; KAS: $\ln(\beta/T^2) = \ln(AR/Eg(\alpha)) - E/RT$.

The conversion rate (α) was calculated using the following formula:

$$\alpha = \frac{m_{\text{onset}} - m_t}{m_i - m_{end}} \quad (1)$$

m_{onset} denotes the initial biomass mass before pyrolysis, g;
m_t denotes the mass at pyrolysis time t, g;
m_{end} denotes the residual mass after pyrolysis, g.

2.5. Characteristic Parameter Extraction and Kinetic Analysis

TG/DTG curves were used to extract characteristic temperatures and DTG-derived indices for comparative evaluation of the blends under N_2. Here, T_{onset} denotes the onset temperature of rapid mass loss (start of major devolatilization), T_p is the DTG peak temperature, and T_{end} denotes the end temperature of major mass loss (completion of devolatilization/transition to slow char evolution). ν_{max} and ν_a represent the maximum and average mass-loss rates, respectively. To enable a direct comparison with prior biomass TGA studies, a comprehensive performance index (S_N) and a reactivity index (R_M) were calculated from these TG/DTG parameters using the same mathematical definitions as Equations (2)–(4); in this work, they are explicitly interpreted as pyrolysis performance indicators (no external oxidant is supplied in N_2).

Based on the aforementioned parameters, the average mass-loss rate (ν) and the comprehensive pyrolysis characteristic index (S_N) can be derived using Equations (2) and (3).

For brevity, standard kinetic derivations and mechanism functions are not repeated here; the procedures follow the established references cited in Section 2.4:

$$\nu_\alpha = \beta \times \frac{\varepsilon_{onset} - \varepsilon_{end}}{T_p - T_{onset}} \quad (2)$$

$$S = \frac{\nu_{\max}\nu_\alpha}{T_{onset}{}^2 T_p} \quad (3)$$

β denotes the heating rate; ε_{onset} and ε_{end} represent the residual mass fractions of the sample corresponding to Tonset and Tend (defined above), respectively:

$$R_M = \frac{DTG_{max}}{T_P} \quad (4)$$

DTGmax denotes the maximum weight loss rate during devolatilization (%/min).
Tp represents the temperature corresponding to the maximum mass-loss rate (°C).

2.6. FTIR Characterization

Fourier-transform infrared spectroscopy (FTIR) was performed to identify major functional groups in CS, SP, and the blends, as well as to verify whether blending induces detectable structural alterations. ATR–FTIR spectra were collected in the range of 4000–400 cm^{-1} with 4 cm^{-1} resolution and 32 scans using the same 18-mesh powders as for TGA. The spectra (baseline-corrected and normalized for comparison) are provided in Figure 3; key bands were assigned to O–H stretching (~3400 cm^{-1}), C–H stretching (2920/2850 cm^{-1}), carbonyl C=O (~1730 cm^{-1}), lignin aromatic skeletal vibrations (1600–1510 cm^{-1}) and polysaccharide C–O–C/C–O (1160–1030 cm^{-1}).

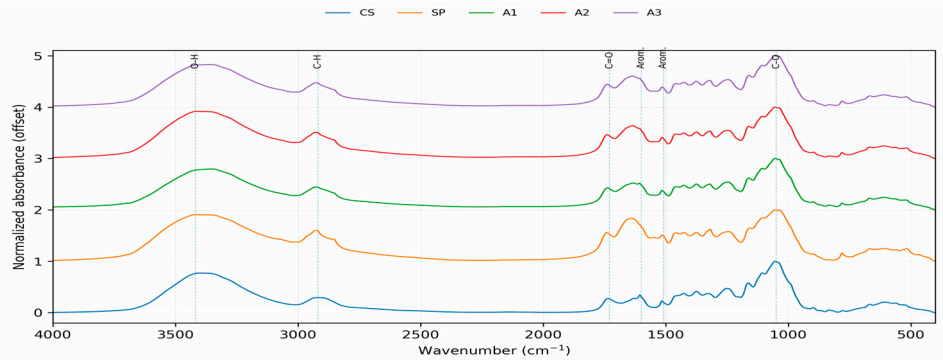


Figure 3. ATR–FTIR spectra of CS, SP and blends (A1–A3) with key band assignments for lignin and polysaccharides.

Figure 3 presents the ATR–FTIR spectra of CS, SP, and the blended samples (A1–A3). All samples exhibit a broad O–H stretching band around ~3400 cm^{-1}, as well as C–H stretching bands at 2920/2850 cm^{-1}, which are characteristic of lignocellulosic biomass [17]. A discernible carbonyl C=O band near ~1730 cm^{-1} is associated with unconjugated carbonyl/ester groups (mainly hemicellulose), while bands in the 1600–1510 cm^{-1} region correspond to aromatic skeletal vibrations of lignin. The polysaccharide-related C–O–C/C–O stretching bands (1160–1030 cm^{-1}) are evident in all spectra [18]. Compared with single feedstocks, the blends show intermediate intensities of hemicellulose- and lignin-related bands, indicating a complementary functional-group distribution that can facilitate staged devolatilization and a more balanced formation of the solid matrix during thermal conversion. These assignments are consistent with recent FTIR studies of lignocellulosic biomass and related thermal conversion materials [19].

2.7. Thermodynamic Parameter Calculation

Thermodynamic parameters are crucial for gaining a deeper understanding of biomass pyrolysis processes; enthalpy change (ΔH), entropy change (ΔS), and Gibbs free energy change (ΔG) are commonly used thermodynamic parameters. Enthalpy change (ΔH) specifically quantifies the energy difference between the original biomass and the activated complex, revealing the amount of heat released or absorbed during the process. Entropy change (ΔS) serves as a comprehensive characteristic describing the disorder state of a

system. In contrast, Gibbs free energy change (ΔG) characterizes the spontaneity of the process [20]. Determining ΔH, ΔS, and ΔG from kinetic parameters involves specific computational methods:

$$\Delta H = E - RT \tag{5}$$

$$\Delta S = R \cdot ln(A \cdot h/(kB \cdot T) \tag{6}$$

$$\Delta G = \Delta H - T\Delta S \tag{7}$$

Using the Eyring transition state framework, thermodynamic parameters of the activation complex were evaluated based on kinetic parameters. At the representative temperature T (K) during the primary desorption phase, the enthalpy change ΔH and entropy change ΔS were determined, where A is the pre-exponential factor (s^{-1}), h is Planck's constant, and kB is the Boltzmann constant. Gibbs free energy change ΔG characterizes the spontaneity of the process. These parameters serve as comparative descriptors for energy barriers and the ordering of activation complexes under inert conditions at different mixing ratios.

3. Results

3.1. SEM Microstructural Characterization

3.1.1. Microstructure of a Single Sample

The SEM images of corn stover (Figure 4) reveal a rough, porous surface with fibers exhibiting some directional alignment. However, the fibers lack tight inter-fiber bonding structures and show distinct separation gaps. High-magnification observation reveals relatively smooth fiber surfaces. This structure tends to result in insufficient forming strength during single-fuel densification and can lead to unstable devolatilization behavior in subsequent thermochemical conversion [21]. *Salix psammophila* exhibits a dense morphology (Figure 5), with few and unevenly distributed surface pores and only minor fine cracks. Inter-fiber bonding is significantly higher than in corn stover, but its dense structure may impede volatile escape during thermal decomposition under N_2.

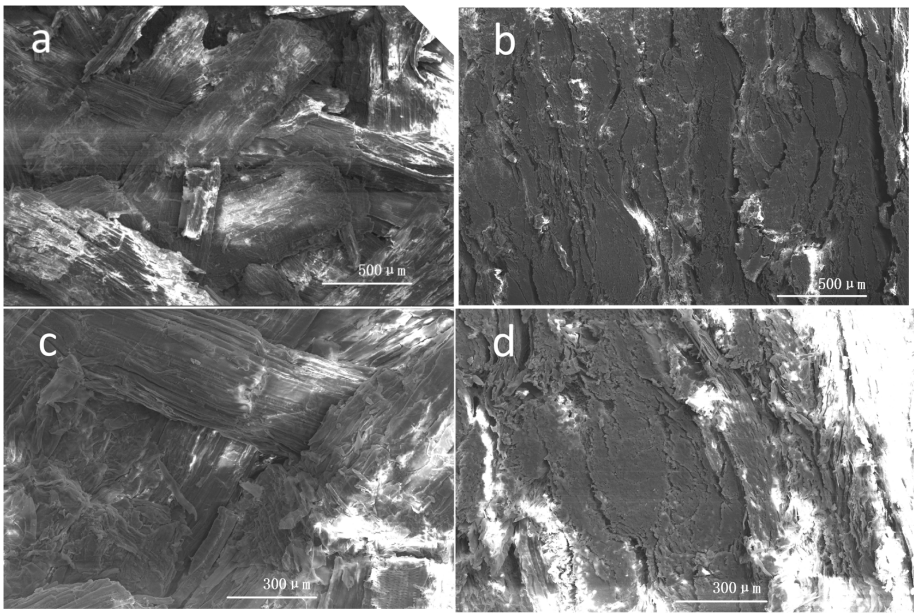


Figure 4. Cross-sectional and lateral SEM figures of corn stover. Key features include loosely bonded fibers, visible inter-fiber gaps (porosity pathways), and relatively smooth fiber surfaces at high magnification: (**a**) 50× cross-sectional magnification; (**b**) 150× cross-sectional magnification; (**c**) 50× side magnification; and (**d**) 150× side magnification.

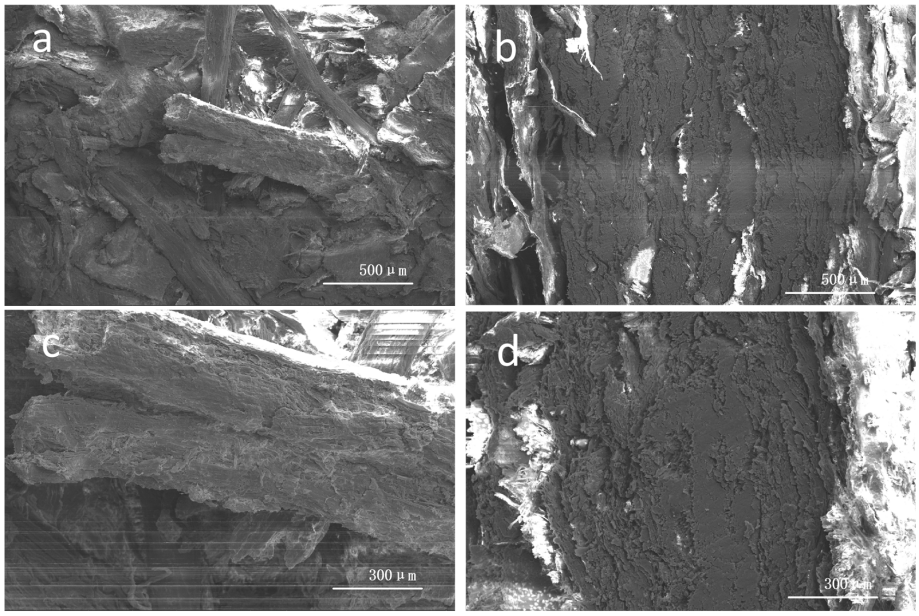


Figure 5. Cross-sectional and lateral SEM figures of *Salix psammophila*. Key features include denser matrix with fewer surface pores, fine cracks, and stronger inter-fiber bonding compared with CS: (**a**) 50× cross-sectional magnification; (**b**) 150× cross-sectional magnification; (**c**) 50× side magnification; and (**d**) 150× side magnification.

3.1.2. Microstructure of the Blended Sample

Note on pore/surface characterization (SEM vs. BET): BET (N_2 adsorption) provides the quantitative specific surface area (SSA) and micro/mesopore distributions, especially for chars and finely ground solids [22]. However, the present samples are raw 18-mesh biomass blends, where dominant voids are micron-scale inter-particle/inter-fiber pores; thus, SEM more directly captures pore connectivity and interfacial contact controlling heat transfer and volatile escape, which are the key structural factors discussed in this work. Due to the Chinese Spring Festival holiday and temporary laboratory shutdown, BET measurements could not be completed during the revision period. SEM evidence and TG/DTG trends together are sufficient to support the ratio-optimization conclusions; BET will be added as complementary data in future work once instrument access is restored [23,24].

Group A1 (2:1): Corn stover fibers form a continuous matrix, with sand willow particles distributed throughout as the dispersed phase, although unevenly and locally aggregated. The interfacial transition layer is narrow (8–10 μm), indicating limited physical crosslinking and loose interface bonding between the two materials, as observed in Figure 6;

Group A2 (3:1): Sand willow particles are uniformly embedded within the corn stover fiber network, as shown in Figure 7. This forms an ideal "continuous phase–dispersed phase" composite structure. The interfacial transition layer reaches 11–15 μm in thickness, with uniformly distributed pores generally smaller than 50 μm. This structure effectively promotes volatile-release diffusion and internal heat transfer, providing structural support for synergistic thermal decomposition under N_2;

Group A3 (5:2): Increased *Salix psammophila* content causes local particle agglomeration, disrupting the "continuous phase–dispersed phase" structure; the interfacial transition layer thins (7–9 μm), with poor pore distribution uniformity and large pores appearing in some areas, which is detrimental to stable devolatilization and char evolution under N_2 [25] (Figures 6–8).

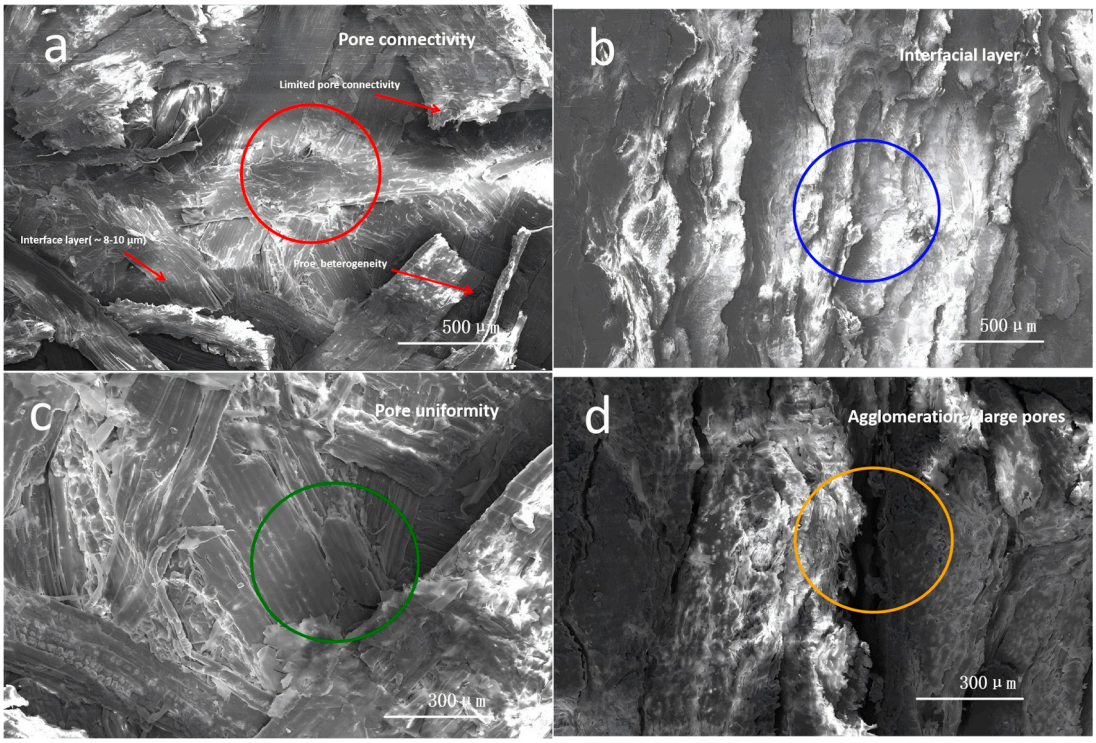


Figure 6. Cross-sectional and lateral SEM figures of hybrid fuel A1 group. Key features include continuous CS fiber phase with dispersed SP particles, local aggregation, and a relatively thin interfacial transition layer (~8–10 μm): (**a**) 50× cross-sectional magnification; (**b**) 150× cross-sectional magnification; (**c**) 50× side magnification; and (**d**) 150× side magnification.

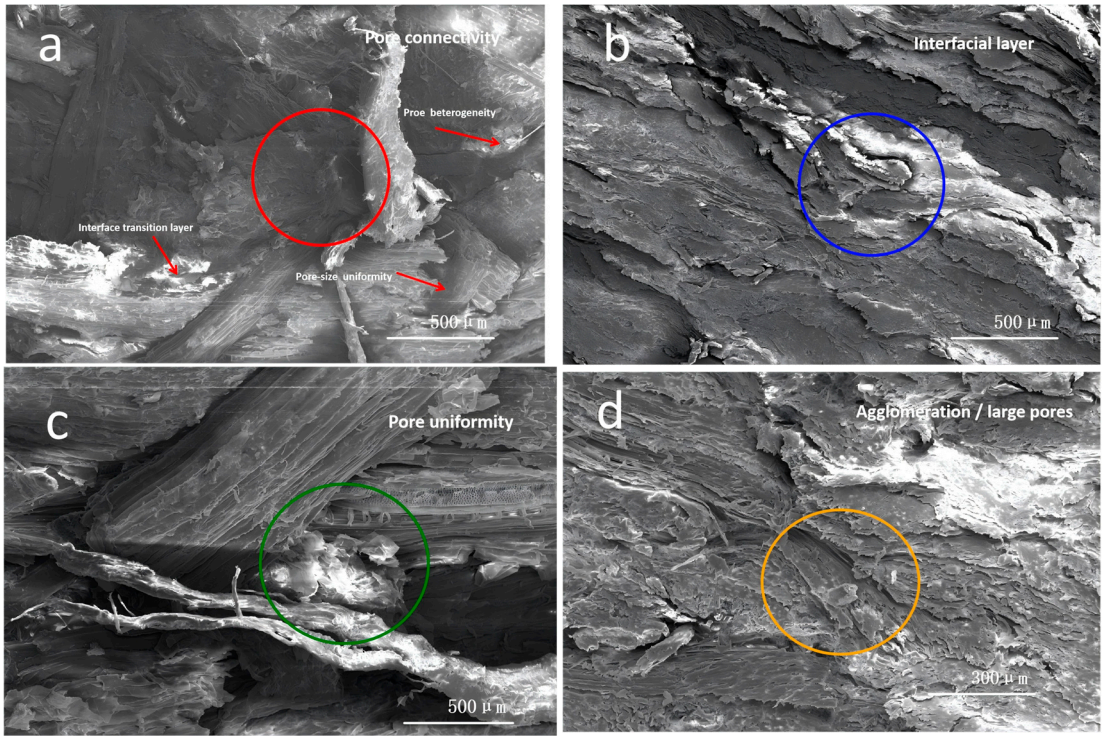


Figure 7. Cross-sectional and lateral SEM figures of hybrid fuel A2 group. Key features include well-dispersed SP particles, thicker interfacial transition layer (~11–15 μm), and uniformly distributed fine pores (<50 μm), indicating improved pore connectivity: (**a**) 50× cross-sectional magnification; (**b**) 150× cross-sectional magnification; (**c**) 50× side magnification; and (**d**) 150× side magnification.

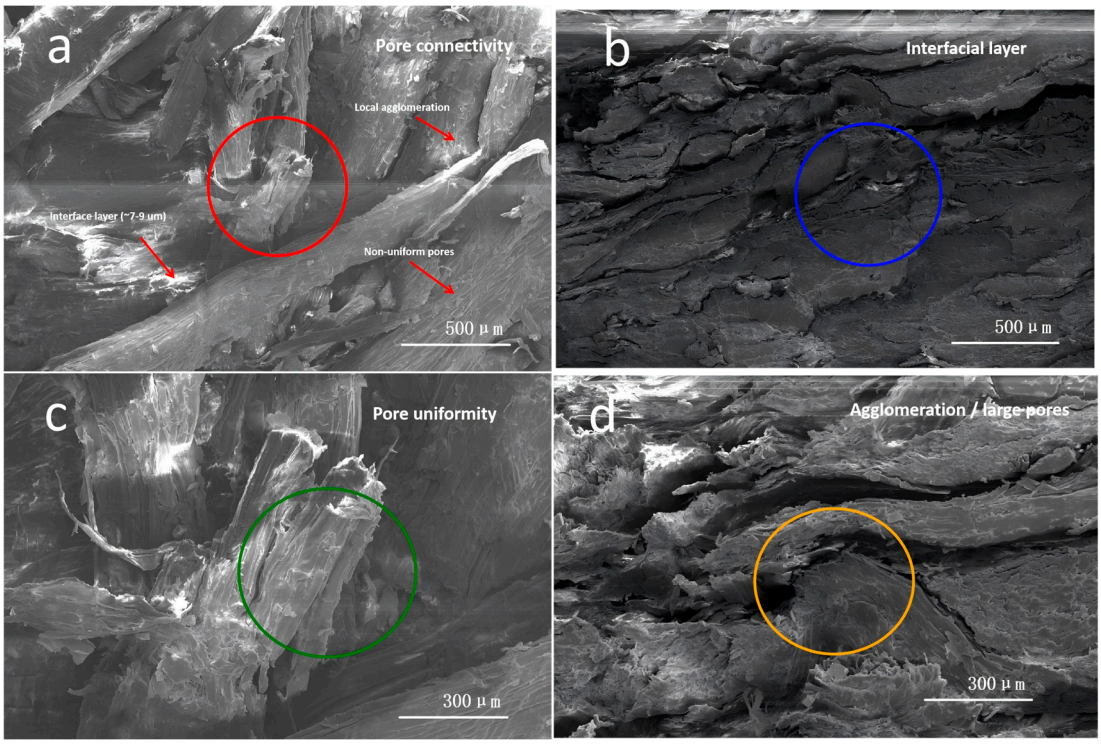


Figure 8. Cross-sectional and lateral SEM figures of hybrid fuel A3 group. Key features include higher SP fraction leading to denser regions, less-uniform pore distribution, and localized compact zones that may hinder volatile escape: (**a**) 50× cross-sectional magnification; (**b**) 150× cross-sectional magnification; (**c**) 50× side magnification; and (**d**) 150× side magnification.

Although BET (N_2 adsorption) can quantify specific surface area and micro/mesopore distributions, its applicability is more straightforward for carbonized materials (chars/biochars) with stable adsorption-accessible pore networks. In the present work, the samples are raw 18-mesh biomass blends, and the structure–reactivity relationship in inert pyrolysis is dominated by micron-scale inter-fiber/inter-particle voids, pore connectivity, and interfacial contact zones formed between SP and CS particles. These features control heat transfer paths and volatile release channels and are directly observable using SEM, enabling intuitive comparison among blending ratios. Therefore, SEM evidence provides an appropriate basis for discussing pore connectivity and interfacial structure in this study. Additional BET measurements will be considered in future work, when adsorption instrumentation becomes available.

3.2. Thermogravimetric (TG/DTG)Analysis of Pyrolysis Characteristics Under N_2

3.2.1. Pyrolysis Characteristics of Single Samples

The thermal decomposition of corn stover and *Salix psammophila* under N_2 can be divided into three stages [26,27]: (i) drying (30–190 °C), dominated by moisture and light extractives release; (ii) devolatilization (200–500 °C), featuring intense decomposition of hemicellulose and cellulose with rapid volatile evolution; and (iii) char formation and slow degradation (500–800 °C), mainly associated with lignin decomposition and progressive carbonization. With the heating rate increasing from 5 to 15 °C·min^{-1}, the main DTG peaks shift to higher temperatures due to thermal lag and νmax increases accordingly. Here, T_{onset} denotes the onset temperature of rapid mass loss (start of major devolatilization). T_p is the DTG peak temperature, and T_{end} denotes the end temperature of major mass loss (completion of devolatilization/transition to slow char evolution). Because SP has a denser structure and higher ash content (Table 1), its T_p and T_{end} are generally higher than CS,

indicating higher thermal stability and a longer char-forming interval under N_2., as shown in Figures 9 and 10.

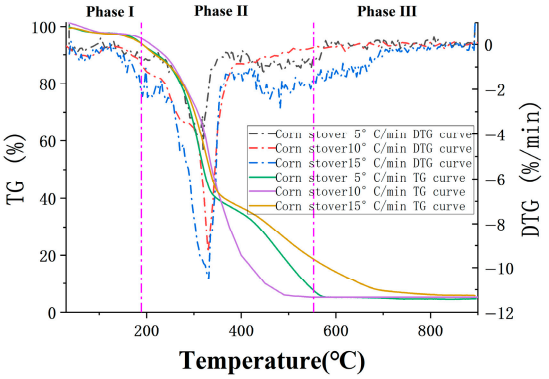


Figure 9. Thermogravimetric curve of corn stover.

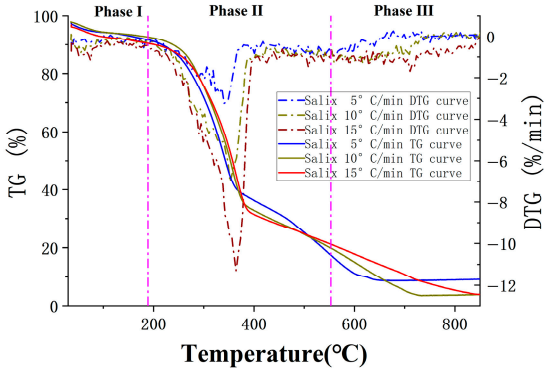


Figure 10. Thermogravimetric curve of salix.

3.2.2. Pyrolysis Characteristics of Mixed Samples

The thermal-decomposition behavior of the blended samples is jointly regulated by the mixing ratio and heating rate. Group A2 (3:1) demonstrated the most favorable pyrolysis indicators across all heating rates (Table 2). At 5 °C·min^{-1} (low heating rate), A2 achieved ν_{max} = 4.671%·min^{-1}, higher than A1 (3.062%·min^{-1}) and A3 (4.068%·min^{-1}); its comprehensive pyrolysis performance index (S_N) was 0.953, representing a 13.2% and 10.9% increase over A1 (0.842) and A3 (0.859), respectively, while the reactivity index (R_M) reached 0.0307%·min^{-1}·°C^{-1}. At 10 °C·min^{-1} (medium rate), A2 showed higher S_N (1.65) than A1 (1.36), with an average mass-loss rate (ν_a) of 2.16%·min^{-1}. The TG curves revealed more complete mass loss during the late char-evolution stage and lower residual mass, attributed to the more uniform pore structure providing ample pathways for volatile diffusion [28,29]. At 15 °C·min^{-1} (high rate), A2 exhibited the lowest T_{onset} (209 °C) among the blends, with S_N reaching 3.01. The DTG peak was more symmetric, with less tailing, indicating a smoother transition from devolatilization to slow char evolution, reducing the localized overheating and coking tendency. Although A3 exhibited the highest νmax (12.519%·min^{-1}), its T_{end} was only 583 °C, suggesting a shorter effective devolatilization interval and less stable late-stage mass-loss behavior (Figures 11–13).

Table 2. TG/DTG-derived characteristic parameters of different samples under N_2 (used for comparative pyrolysis evaluation).

Sample	Heating Rate (°C·min^{-1})	T_{onset} (°C)	T_p (°C)	ν_{max} (%·min^{-1})	T_{end} (°C)	ν_a (%·min^{-1})	ε (%)	S_N (×10^6)	R_M (%·min^{-1}·°C^{-1})
SP	5	252	340.31	3.247	450	2.21	11.2	0.33	0.0128
	10	238	352.52	7.033	578	2.79	5.16	0.99	0.296
	15	222	364.13	11.285	678	3.07	5.76	1.66	0.0452
CS	5	247	319.17	4.705	432	1.91	11.26	1.18	0.019
	10	230	331.38	9.297	559	2.66	5.27	2.01	0.0465
	15	208	340.44	10.502	636	2.91	5.79	2.82	0.0607
A1	5	249	322.61	3.062	463	1.02	11.45	0.842	0.027
	10	236	334.35	8.594	536	2.11	11.78	1.36	0.0394
	15	217	303.9	9.448	591	3.31	11.24	2.59	0.0519
A2	5	256	319.45	4.671	482	1.04	5.35	0.953	0.0307
	10	243	331.35	8.045	569	2.16	6.78	1.65	0.0438
	15	209	328.54	10.249	607	3.37	6.08	3.01	0.0565
A3	5	246	312.68	4.068	471	1.03	11.06	0.859	0.0268
	10	235	332	7.773	540	2.13	2.68	1.48	0.0465
	15	213	326.31	12.519	583	3.34	2.88	2.66	0.0517

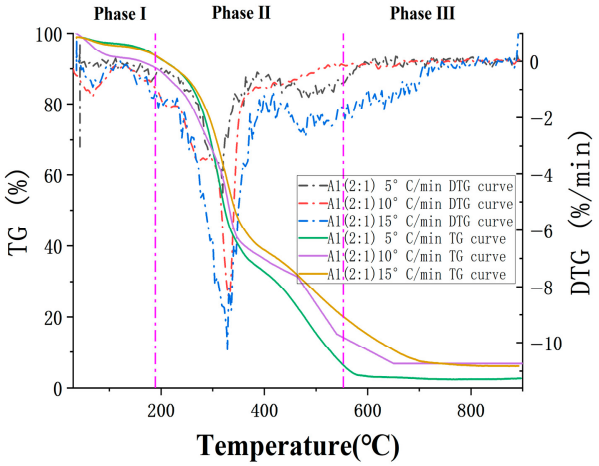


Figure 11. TG/DTG curves of group A1 under N_2.

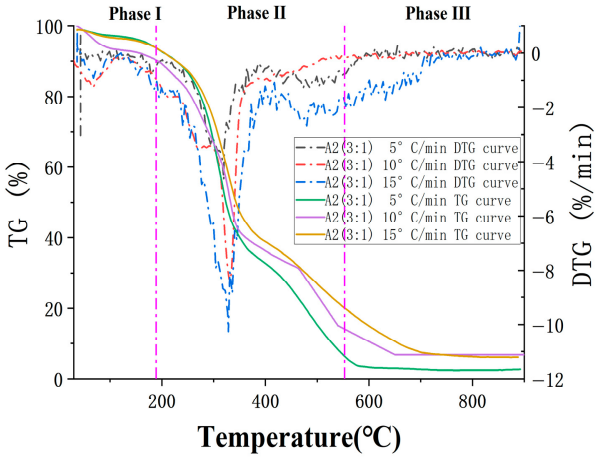


Figure 12. TG/DTG curves of group A2 under N_2.

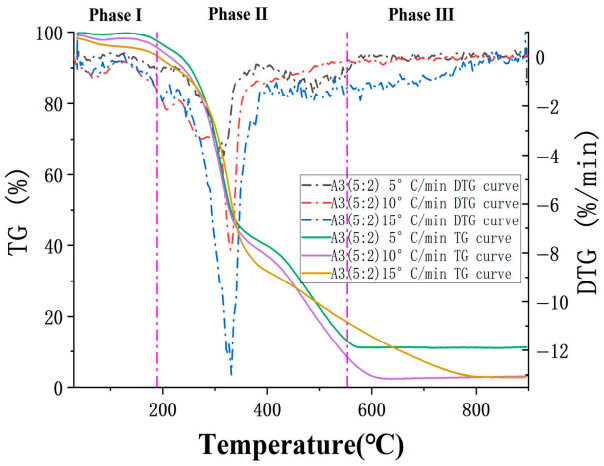


Figure 13. TG/DTG curves of group A3 under N_2.

3.3. Pyrolysis Kinetic Analysis Under N_2

3.3.1. Coats–Redfern Integration Method

The kinetic fitting parameters for the three mixed samples during the three thermal-decomposition stages under N_2 (drying, devolatilization and char-formation/slow degradation) are shown in Table 3. The correlation coefficients (R^2) for all samples were ≥0.95, indicating a significant linear relationship and high model reliability [30]. The fitting curves are presented in Figures 14–16. The stages are presented below.

Table 3. Kinetic fitting parameters of mixed samples.

Phase	Heating Rate °C/min	Mixed Sample	Fitting Formula	E/(KJ mol^{-1})	A/min^{-1}	R^2
Phase One	5	A1	Y = −1820X − 5.88	15.16	24.52	0.96
		A2	Y = −1720X − 5.55	14.35	33.82	0.97
		A3	Y = −1950X − 5.98	16.22	24.42	0.95
	10	A1	Y = −1980X − 6.05	16.46	48.62	0.97
		A2	Y = −1850X − 5.72	15.38	61.12	0.98
		A3	Y = −2100X − 6.25	17.46	40.84	0.96
	15	A1	Y = −2150X − 6.28	17.97	60.70	0.98
		A2	Y = −2000X − 6.05	16.65	75.73	0.98
		A3	Y = −2250X − 6.42	18.76	53.88	0.97
Phase Two	5	A1	Y = −6200X − 3.55	51.58	879.13	0.98
		A2	Y = −5900X − 3.42	49.13	963.12	0.99
		A3	Y = −6500X − 3.64	56.53	841.11	0.97
	10	A1	Y = −6550X − 3.72	54.45	1608.00	0.99
		A2	Y = −6200X − 3.58	51.54	1703.45	0.99
		A3	Y = −6800X − 3.82	54.03	1467.88	0.98
	15	A1	Y = −6900X − 3.98	57.41	1911.41	0.99
		A2	Y = −6500X − 3.85	54.09	2075.17	0.99
		A3	Y = −7100X − 4.05	59.31	1760.34	0.99
Phase Three	5	A1	Y = −12,300X − 1.85	102.35	9626.02	0.97
		A2	Y = −12,000X − 1.82	99.86	9678.17	0.98
		A3	Y = −12,800X − 1.92	106.49	9320.22	0.98
	10	A1	Y = −12,800X − 2.02	106.41	17,083.25	0.98
		A2	Y = −12,500X − 1.98	103.93	17,298.99	0.98
		A3	Y = −13,200X − 2.15	109.75	15,345.33	0.99
	15	A1	Y = −13,300X − 2.25	110.62	20,916.62	0.99
		A2	Y = −13,000X − 2.22	108.11	20,667.31	0.99
		A3	Y = −13,500X − 2.30	112.26	20,074.48	0.99

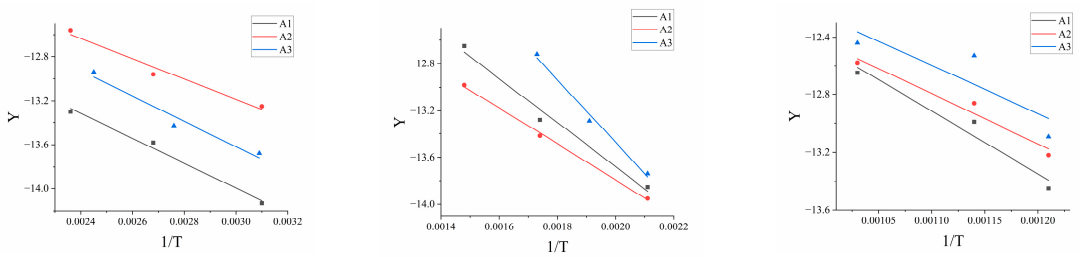


Figure 14. Coats–Redfern fitting curves for three mixed fuel groups at a heating rate of 5 °C/min: (**a**) phase one; (**b**) phase two; and (**c**) phase three.

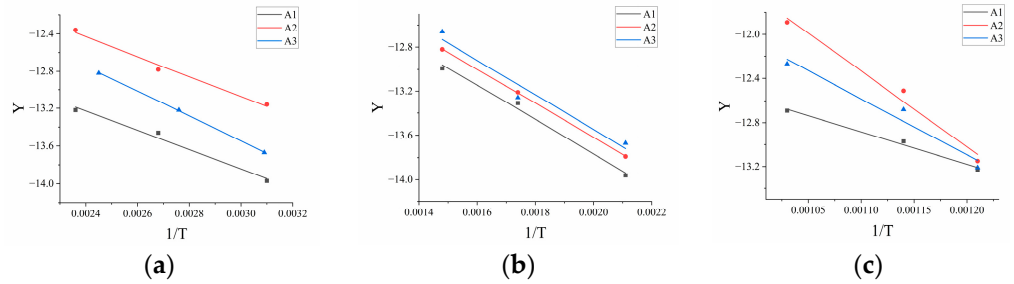


Figure 15. Coats–Redfern fitting curves for three mixed fuel groups at a heating rate of 10 °C/min: (**a**) phase one; (**b**) phase two; and (**c**) phase three.

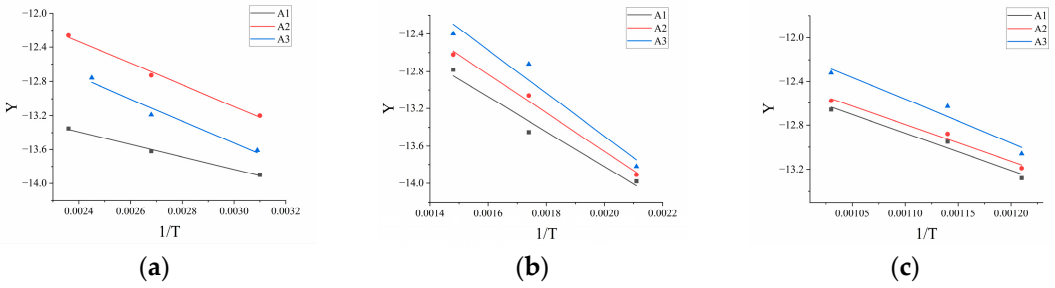


Figure 16. Coats–Redfern fitting curves for three mixed fuel groups at a heating rate of 15 °C/min: (**a**) phase one; (**b**) phase two; and (**c**) phase three.

The drying stage primarily involves moisture volatilization, with generally low activation energies (E) (14–19 kJ/mol). Group A2 exhibited E = 14.35 kJ/mol at 5 °C·min^{-1}, slightly lower than Groups A1 and A3, indicating reduced energy consumption for moisture removal [31]. The devolatilization stage is the core thermal-decomposition interval, where E significantly increases (49–59 kJ/mol) due to the intense breakdown of hemicellulose/cellulose and rapid volatile release. At 5 °C·min^{-1}, Group A2 exhibits E = 49.13 kJ/mol, lower than Groups A1 (51.58 kJ/mol) and A3 (56.53 kJ/mol), indicating this formulation reduces the energy barrier for devolatilization reactions and accelerates volatile release. The char-formation/slow degradation stage is the most complex thermal-decomposition interval (often affected by mineral-matter shielding and secondary reactions), with the highest apparent activation energies (99–112 kJ/mol). Group A2 exhibited E = 99.86 kJ/mol at 5 °C·min^{-1}, still lower than the other two groups, confirming that its char evolution proceeded more readily under N_2. The parameters are shown in Table 3.

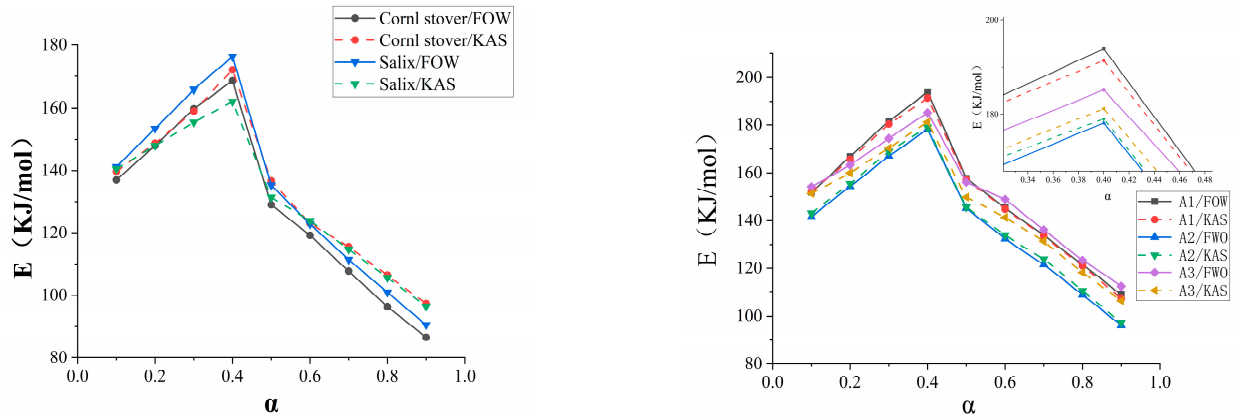
3.3.2. FWO and KAS Method Verification

Using the FWO and KAS model-free methods, kinetic parameters were calculated at conversion rates α = 0.1–0.9 (gradient 0.1) to validate the reliability of the Coats–Redfern method results (Table 4). The calculated results from both methods showed minimal

discrepancy [32–34]. Under the FWO method, the average activation energy for Group A2 was 138.39 kJ/mol, significantly lower than that of Group A1 (151.26 kJ/mol) and Group A3 (150.43 kJ/mol). Under the KAS method, the average activation energy for Group A2 was 139.88 kJ/mol, highly consistent with the FWO method results. The comparison of activation energies obtained from the two fitting methods is shown in Figure 17.

Table 4. Kinetic parameters of FWO and KAS methods.

α	CS		SP		A1		A2		A3	
	FWO	KAS	FWO	KAS	FWO	KAS	FWO	KAS	FWO	KAS
0.1	137.3	139.7	141.2	140.5	151.8	152.2	146.5	143.6	154.2	151.3
0.2	147.7	148.8	153.5	148.8	166.8	165.6	154.3	155.5	163.3	160.8
0.3	159.8	160.5	165.8	155.5	181.6	180.3	167.5	168.9	174.3	170.4
0.4	168.2	172.6	176.2	162.1	193.9	191.4	175.1	179.8	185.2	181.2
0.5	129.5	136.7	135.3	131.4	157.8	157.2	143.1	145.5	156.1	149.7
0.6	119.1	123.4	122.8	123.9	145.1	144.7	132.4	133.8	148.8	141.3
0.7	107.7	115.5	111.4	114.7	133.9	133.5	121.5	123.9	136.1	131.4
0.8	96.3	106.4	100.9	105.6	121.5	120.9	108.9	110.6	123.4	118.1
0.9	86.5	97.3	90.5	96.4	108.9	107.3	96.2	97.3	112.5	106.4



(**a**) (**b**)

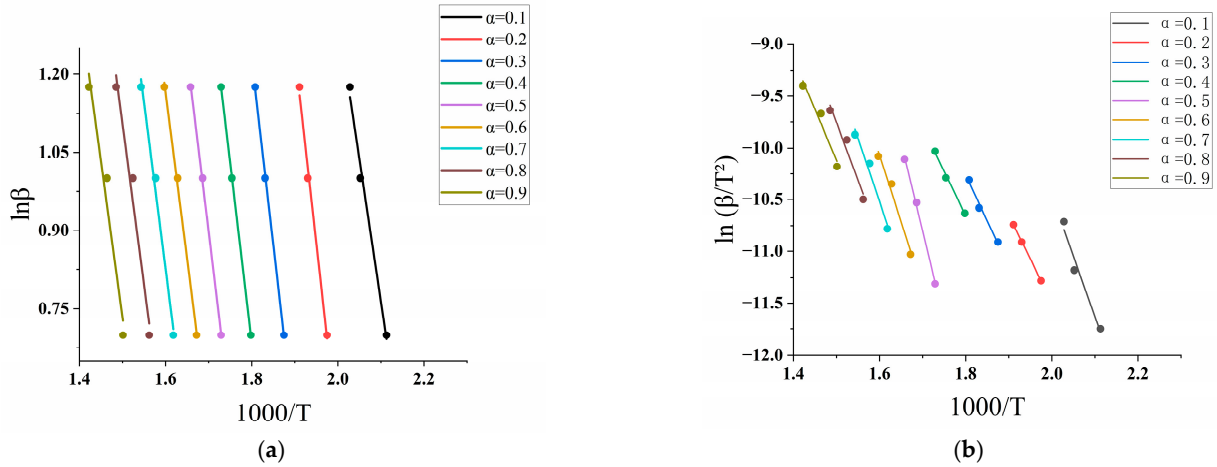
Figure 17. Comparison of activation energies obtained from FWO and KAS methods: (**a**) corn stover and *Salix psammophila*; and (**b**) mixed samples A1–A3.

The activation energy for all samples exhibited a "first increase, then decrease" trend with increases in the conversion rate [35]. During α = 0.1–0.4, the activation energy increased, corresponding to the initial devolatilization phase (light volatiles release and intense decomposition of hemicellulose/cellulose). During α = 0.5–0.9, the activation energy decreased, corresponding to the late-stage char evolution/slow degradation interval under N_2 (reduced reaction difficulty as reactive sites become more accessible and secondary reactions diminish) [36].

Based on Table 5, the activation energies for the FWO and KAS model-free methods can be calculated for different biomass fuel mixtures. The resulting fitted curves are shown in Figures 18–20. The symbols correspond to experimental points extracted at β = 5, 10 and 15 °C·min^{-1}; solid lines are linear fits for α = 0.1–0.9. The fit equations and R^2 are reported in Table 5.

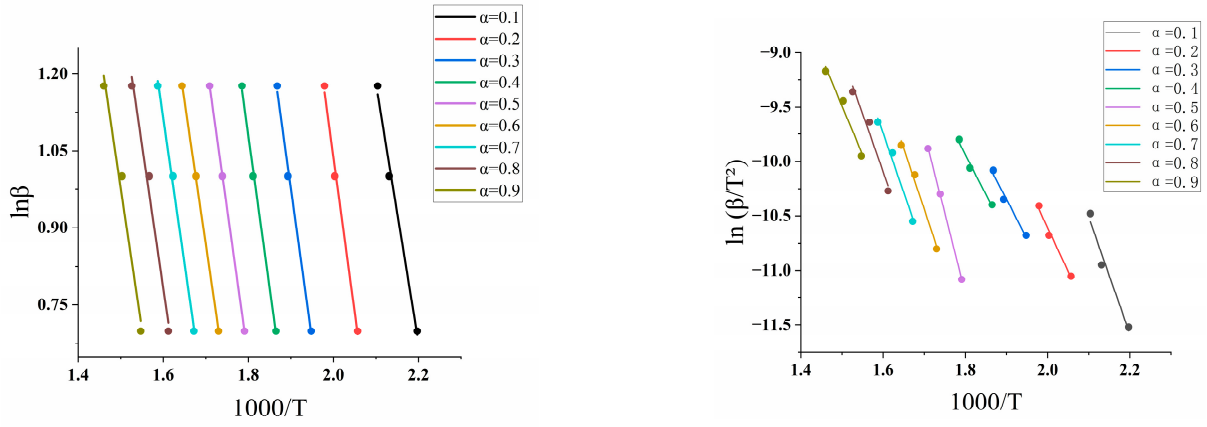
Table 5. Linear regression equations and coefficients (R^2) of the FWO and KAS isoconversional fits for blends A1–A3 (α = 0.1–0.9).

Sample	α	FWO Fit (y = ax + b)	FWO R^2	KAS Fit (y = ax + b)	KAS R^2
A1	0.1	y = −8.4x + 17.5	0.98827	y = −18.3x + 25.2	0.98246
A1	0.2	y = −9.2x + 18.3	0.99768	y = −19.9x + 26.8	0.98236
A1	0.3	y = −10.0x + 18.8	0.96077	y = −21.6x + 28.7	0.95831
A1	0.4	y = −10.7x + 19.5	0.97548	y = −23.0x + 29.3	0.95678
A1	0.5	y = −8.7x + 15.1	0.98182	y = −18.9x + 20.9	0.97926
A1	0.6	y = −8.0x + 13.4	0.94722	y = −17.4x + 18.5	0.95791
A1	0.7	y = −7.4x + 12.3	0.94759	y = −16.1x + 15.8	0.95819
A1	0.8	y = −6.7x + 10.8	0.96545	y = −14.5x + 12.7	0.97125
A1	0.9	y = −6.0x + 9.2	0.96697	y = −12.9x + 8.2	0.96151
A2	0.1	y = −7.8x + 16.1	0.99607	y = −17.2x + 24.2	0.99821
A2	0.2	y = −8.5x + 17.0	0.98168	y = −18.7x + 25.9	0.92556
A2	0.3	y = −9.2x + 17.6	0.96616	y = −20.2x + 27.8	0.95716
A2	0.4	y = −9.8x + 18.2	0.99752	y = −21.5x + 28.4	0.94584
A2	0.5	y = −8.0x + 14.4	0.96028	y = −17.5x + 20.1	0.96767
A2	0.6	y = −7.3x + 12.6	0.97571	y = −16.2x + 17.9	0.97121
A2	0.7	y = −6.7x + 11.5	0.96995	y = −14.9x + 15.1	0.96432
A2	0.8	y = −6.0x + 10.0	0.94801	y = −13.3x + 12.0	0.94602
A2	0.9	y = −5.3x + 8.4	0.94445	y = −11.7x + 7.6	0.95742
A3	0.1	y = −8.5x + 18.2	0.99607	y = −18.2x + 25.9	0.99342
A3	0.2	y = −9.0x + 18.3	0.98168	y = −19.2x + 27.1	0.96737
A3	0.3	y = −9.6x + 18.8	0.96616	y = −20.5x + 28.3	0.98273
A3	0.4	y = −10.2x + 19.1	0.99752	y = −21.8x + 29.0	0.98726
A3	0.5	y = −8.6x + 15.2	0.96028	y = −18.0x + 21.3	0.98793
A3	0.6	y = −8.2x + 14.1	0.97571	y = −17.0x + 18.9	0.97357
A3	0.7	y = −7.5x + 12.5	0.96995	y = −15.8x + 16.5	0.94353
A3	0.8	y = −6.8x + 11.0	0.94801	y = −14.2x + 13.2	0.97226
A3	0.9	y = −6.2x + 9.6	0.94445	y = −12.8x + 8.9	0.94893



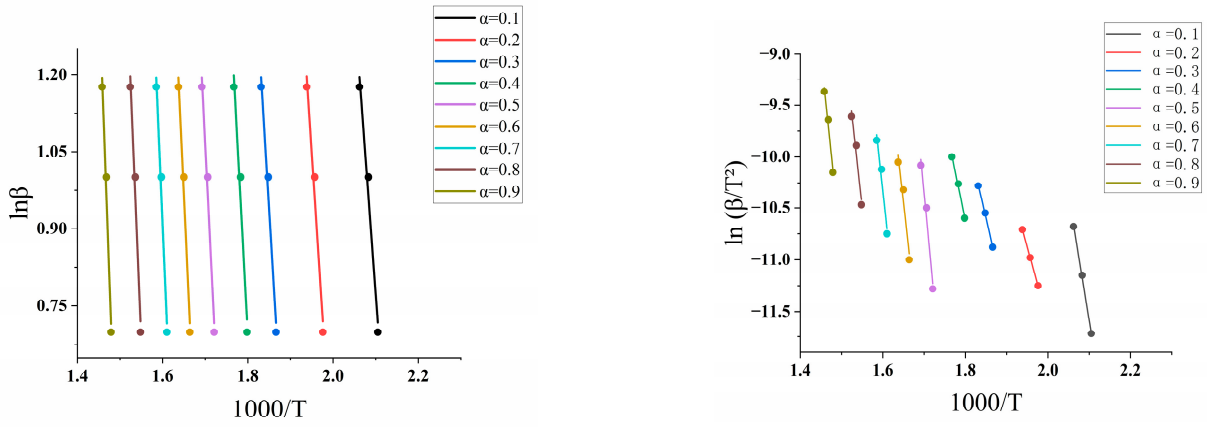
(**a**) (**b**)

Figure 18. Fitting curves for the FWO method and KAS method in Group A1: (**a**) A1 Group FWO fitting curve; and (**b**) KAS method fitted curve for Group A1.



(**a**) (**b**)

Figure 19. Fitting curves for the FWO method and KAS method in Group A2: (**a**) A2 Group FWO fitting curve; and (**b**) KAS method fitted curve for Group A2.



(**a**) (**b**)

Figure 20. Fitting curves for the FWO method and KAS method in Group A3: (**a**) A3 Group FWO fitting curve; and (**b**) KAS method fitted curve for Group A3.

3.3.3. Thermodynamic Analysis

To further interpret the blending effect from an energetic perspective, ΔH, ΔS and ΔG for the main devolatilization stage (Phase Two) were calculated using Equations (5)–(7), based on the Coats–Redfern kinetic parameters (Table 3) and Tp from the TG/DTG analysis (Table 2). The calculated values are summarized in Table 6.

Thermodynamic parameters (ΔH, ΔS and ΔG) of the activated complex for Phase One–Three were calculated using Equations (5)–(7) based on the stage-wise kinetic parameters (Table 3) and the characteristic temperatures (Table 2), as summarized in Table 6.

ΔH is positive in all phases and increases from Phase One (9.95–14.72 kJ·mol^{-1}) to Phase Two (44.20–54.33 kJ·mol^{-1}) and further to Phase Three (93.58–105.14 kJ·mol^{-1}), indicating that formation of the activated complex becomes progressively more endothermic as thermal decomposition proceeds from initial devolatilization to late-stage char evolution under N_2. ΔS is consistently negative in all phases (Phase One: −257.01 to −246.97 J·mol^{-1}·K^{-1}; Phase Two: −228.57 to −221.29 J·mol^{-1}·K^{-1}; Phase Three: −210.57 to −205.09 J·mol^{-1}·K^{-1}), suggesting that the activated complex is more ordered than the reactant ensemble, which is consistent with constrained bond scission/rearrangement within the lignocellulosic matrix during volatile release and subsequent char transformation.

Table 6. Thermodynamic parameters for Phase One–Three calculated using Equations (5)–(7) under N_2. Characteristic temperatures T* were taken as the Tonset (Phase One), Tp (Phase Two) and Tend (Phase Three) from Table 2 for each heating rate.

Phase	Sample	β (°C·min^{-1})	T* (K)	E (kJ·mol^{-1})	A (min^{-1})	ΔH (kJ·mol^{-1})	ΔS (J·mol^{-1}·K^{-1})	ΔG (kJ·mol^{-1})
Phase One	A1	5	522.15	15.16	24.52	10.82	−257.01	145.02
Phase One	A1	10	509.15	16.46	48.62	12.23	−251.11	140.08
Phase One	A1	15	490.15	17.97	60.7	13.89	−248.95	135.92
Phase One	A2	5	529.15	14.35	33.82	9.95	−254.45	144.59
Phase One	A2	10	516.15	15.38	61.12	11.09	−249.32	139.77
Phase One	A2	15	482.15	16.65	75.73	12.64	−246.97	131.72
Phase One	A3	5	519.15	16.22	24.42	11.9	−256.99	145.32
Phase One	A3	10	508.15	17.46	40.84	13.24	−252.54	141.56
Phase One	A3	15	486.15	18.76	53.88	14.72	−249.87	136.19
Phase Two	A1	5	595.76	51.58	879.13	46.63	−228.35	182.67
Phase Two	A1	10	607.5	54.45	1608.0	49.4	−223.49	185.17
Phase Two	A1	15	577.05	57.41	1911.41	52.61	−221.62	180.5
Phase Two	A2	5	592.6	49.13	963.12	44.2	−227.54	179.05
Phase Two	A2	10	604.5	51.54	1703.45	46.51	−222.97	181.3
Phase Two	A2	15	601.69	54.09	2075.17	49.09	−221.29	182.23
Phase Two	A3	5	585.83	56.53	841.11	51.66	−228.57	185.56
Phase Two	A3	10	605.15	54.03	1467.88	49.0	−224.21	184.68
Phase Two	A3	15	599.46	59.31	1760.34	54.33	−222.62	187.78
Phase Three	A1	5	736.15	102.35	9626.02	96.23	−210.21	250.97
Phase Three	A1	10	809.15	106.41	17,083.25	99.68	−206.22	266.55
Phase Three	A1	15	864.15	110.62	20,916.62	103.44	−205.09	280.66
Phase Three	A2	5	755.15	99.86	9678.17	93.58	−210.37	252.45
Phase Three	A2	10	842.15	103.93	17,298.99	96.93	−206.45	270.79
Phase Three	A2	15	880.15	108.11	20,667.31	100.79	−205.34	281.52
Phase Three	A3	5	744.15	106.49	9320.22	100.3	−210.57	257.0
Phase Three	A3	10	813.15	109.75	15,345.33	102.99	−207.16	271.44
Phase Three	A3	15	856.15	112.26	20,074.48	105.14	−205.35	280.95

T* denotes the thermodynamic temperature converted from the Celsius value of Tonset in Table 2. T* (K) = T_{onset} (°C) + 273.15.

ΔG remains positive in all cases (Phase One: 131.72–145.32 kJ·mol^{-1}; Phase Two: 179.05–187.78 kJ·mol^{-1}; Phase Three: 250.97–281.52 kJ·mol^{-1}). Here, ΔG is interpreted as the free-energy requirement to reach the activated complex (a kinetic barrier descriptor) rather than the overall feasibility of biomass conversion. Among the blends, A2 exhibits the lowest average ΔG in both Phase One and the main devolatilization stage (Phase Two), with Phase Two showing an average ΔG of 180.86 kJ·mol^{-1} (vs. 182.78 for A1 and 186.01 for A3), indicating a reduced effective barrier and a higher reaction probability. In Phase Three, A1 shows a slightly lower ΔG than A2, but the difference is small and does not change the ratio optimization because Phase Two dominates volatile release and governs the overall process intensity. Therefore, the thermodynamic descriptors provide an energetic explanation consistent with the observed synergistic behavior, supporting the 3:1 (A2) ratio as the optimal blend under N_2.

3.4. Synergistic Pyrolysis Mechanism and Ratio Optimization

The optimal pyrolysis performance of Group A2 (3:1) stems from multidimensional synergies among "component complementarity–microstructure–kinetics" under N_2: (i) Component complementarity: CS (high volatile matter) promotes earlier devolatilization, while SP (higher lignin and HHV) strengthens the char-forming framework and mitigates excessive melt/coking propensity in CS [37]; (ii) Microstructural advantage: the "continuous phase–dispersed phase" structure with an 11–15 μm interfacial transition layer enhances physical interlocking between fibers and particles, while more homogeneous pores (<50 μm) provide effective channels for heat transfer and volatile escape, reducing local overheating [38]; and (iii) Kinetic advantage: the lower apparent activation energy in the devolatilization stage (49.13 kJ/mol at 5 °C/min) lowers the energy barrier for volatile evolution, while a higher pre-exponential factor increases reaction probability [39]. Future work will extend the present inert N_2 pyrolysis analysis to a separate staged conversion scheme (pyrolysis in N_2 followed by controlled oxidation in a dedicated step) and quantify gas/pollutant formation; these oxidative results are beyond the scope of this manuscript.

Mechanism summary (Figure 21): The blending effect under N_2 is governed by an interface-assisted devolatilization mechanism. CS-derived volatiles evolve rapidly and create local pore pathways, while SP contributes a more rigid lignin-rich matrix that stabilizes the solid framework. At the optimized 3:1 ratio, the interfacial transition layer and uniform micro-pores promote coupled heat transfer and mass transfer, suppressing local agglomeration and enabling smoother staged mass loss; this structural synergy is consistent with the reduced kinetic barrier in the main devolatilization stage.

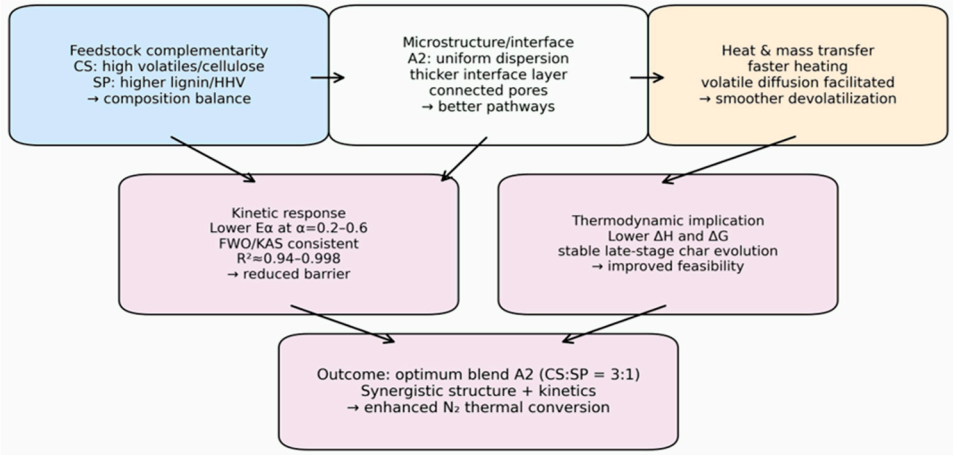


Figure 21. Proposed mechanism scheme for biomass blending effects under N_2 atmosphere (boxed workflow).

4. Conclusions

(1) Under an N_2 atmosphere, the (CS): (SP)ratio of 3:1 (Group A2) formed an ideal "continuous phase-dispersed phase" composite structure. The interfacial transition layer thickness ranged from 11 to 15 μm, with uniformly distributed pores smaller than 50 μm. This structure efficiently promoted heat conduction and volatile-release/mass-transfer pathways, providing structural support for co-pyrolysis synergistic effects;

(2) Group A2 exhibits optimal pyrolysis (thermal conversion) performance at a heating rate of 15 °C/min, low T_{onset} temperature (209 °C), high comprehensive pyrolysis performance index S_N (3.01), stable DTG peaks, smooth transition between volatilize desorption and late-stage char evolution stages, and high conversion stability. This avoids the insufficient molding strength of Group A1 and localized coking issues in Group A3;

(3) Validation via Coats–Redfern, FWO, and KAS methods indicates that Group A2 exhibits the lowest activation energy during the devolatilization stage (49.13 kJ/mol at 5 °C/min) and a significantly lower average activation energy (138.39 kJ/mol) compared to other formulations, making it the most readily initiated thermal decomposition reaction with the highest reaction propensity under N_2;

(4) FTIR results confirm the compositional complementarity of CS- and SP-derived lignocellulosic structures and indicate that interfacial coupling is associated with the concerted evolution of key functional groups (e.g., hydroxyl/carbonyl/ether and aromatic-related bands), supporting the proposed interaction-assisted devolatilization behavior of the blended system;

(5) The multi-method verification (Coats–Redfern, FWO, and KAS) indicates that Group A2 shows the lowest kinetic barrier among the blends (e.g., the lowest average activation energy by FWO), implying the most readily initiated thermal decomposition and the highest reaction probability. Thermodynamic analysis (ΔH, ΔS, and ΔG) further supports that A2 presents a comparatively more favorable energy requirement for the overall conversion under inert conditions;

(6) The 3:1 ratio achieves synergistic effects of "high volatility for facile devolatilization" and "high calorific value for maintaining a stable char framework and mitigating local agglomeration/coking tendency." This ratio is recommended for industrial applications in N_2-based thermochemical conversion (pyrolysis/staged processes), paired with a heating rate of 10–15 °C/min, to maximize the energy utilization value of biomass mixed fuels; further work will incorporate additional heating rates and complementary pore-structure characterization to strengthen statistical robustness.

The NETZSCH STA 449 F3 Jupiter serves as the reaction apparatus for TG/DTG pyrolysis experiments. Although real-time video of the pyrolysis process was not recorded, all experiments were personally conducted by the author following standardized operating procedures. Each sample underwent triplicate testing at every heating rate to validate reproducibility and accuracy (see Section 2.4 for detailed reproducibility metrics).

Author Contributions: Z.L.: Conceptualization, Methodology, Funding Acquisition, Resources; H.F.: Writing—Original Draft, Writing—Review and Editing, Formal Analysis, Investigation, Data Curation; J.Y.: Software, Validation, Resources; H.W.: Project Administration, Writing—Review and Editing; W.W.: Formal Analysis, Writing—Review and Editing; C.F.: Supervision, Funding Acquisition. All authors have read and agreed to the published version of the manuscript.

Funding: National Natural Science Foundation of China (52366018); Inner Mongolia Natural Science Gold (2025MS05072) Basic Research Operating Expenses of Colleges and Universities (2024RCTD006).

Institutional Review Board Statement: Not applicable.

Informed Consent Statement: Not applicable.

Data Availability Statement: The original contributions presented in this study are included in the article. Further inquiries can be directed to the corresponding author.

Conflicts of Interest: The authors declare no conflicts of interest.

Abbreviations

The following abbreviations are used in this manuscript:CS, corn stover; SP, *Salix psammophila*; TGA, thermogravimetric analysis; DTG, derivative thermogravimetry; SEM, scanning electron microscopy; FTIR, Fourier-transform infrared spectroscopy; FWO, Flynn–Wall–Ozawa; KAS, Kissinger–Akahira–Sunose; T_{onset}, onset temperature of major mass loss; T_p, DTG peak temperature; T_{end}, end temperature of major mass loss; ν_{max}, maximum mass-loss rate; ν_a, average mass-loss rate; S_N, comprehensive

pyrolysis performance index; R_M, reactivity index; E, apparent activation energy; A, pre-exponential factor; ΔH, enthalpy change; ΔS, entropy change; ΔG, Gibbs free energy change.

References

1. Liu, L.; Pang, Y.; Lv, D.; Wang, K.; Wang, Y. Thermal and kinetic analyzing of pyrolysis and thermal decomposition of self -heating biomass particles. *Process Saf. Environ. Prot.* **2021**, *151*, 39–50. [CrossRef]
2. Al-Ghussain, L.; Abubaker, A.M.; Ahmad, A.D. Superposition of renewable-energy supply from multiple sites maximizes demand-matching: Towards 100% renewable grids in 2050. *Appl. Energy* **2021**, *284*, 116402. [CrossRef]
3. Niu, Z.Z.; Kong, S.F.; Yan, Q.; Zheng, S.-R.; Zheng, H.; Zeng, X.; Yao, L.-Q.; Wu, J.; Zhang, Y.; Wu, F.-Q.; et al. Profile Characteristics of VOCs from Wood and Economic Crop Burning. *Huan Jing Ke Xue* **2020**, *41*, 1107–1115. [CrossRef]
4. Hong, J.; Ren, L.; Hong, J.; Xu, C. Environmental impact assessment of corn straw utilization in China. *J. Clean. Prod.* **2016**, *112*, 1700–1708. [CrossRef]
5. Liu, Q.M.; Chmely, S.C.; Abdoulmoumine, N. Biomass Treatment Strategies for Thermochemical Conversion. *Energy Fuels* **2017**, *31*, 3525–3536. [CrossRef]
6. Nawaz, A.; Kumar, P. Elucidating the bioenergy potential of raw, hydrothermally carbonized and torrefied waste Arundo donax biomass in terms of physicochemical characterization, kinetic and thermodynamic parameters. *Renew. Energy* **2022**, *187*, 844–856. [CrossRef]
7. Sheng, C.; Yao, Z.; Zhao, L.; Meng, H.; Dai, M.; Cong, H. Mixed molding and thermal decomposition characteristics of cotton stalk char and biomass tar. *J. Sol. Energy* **2022**, *43*, 458–464. [CrossRef]
8. Ahmed, I.; Zia, M.A.; Afzal, H.; Ahmed, S.; Ahmad, M.; Akram, Z.; Sher, F.; Iqbal, H.M.N. Socio-economic and environmental impacts of biomass valorisation: A strategic drive for sustainable bioeconomy. *Sustainability* **2021**, *13*, 4200. [CrossRef]
9. Li, S.; Li, F.; Yan, Y.; Qian, X. A review of research methods for thermal decomposition characterization of single -particle fuels. *Chin. J. Electr. Eng.* **2021**, *41*, 4182–4198. [CrossRef]
10. Skeen, S.A.; Kumfer, B.M.; Axelbaum, R.L. Nitric Oxide Emissions during Coal and Coal/Biomass thermal decomposition under Air-Fired and Oxy-fuel Conditions. *Energy Fuels* **2010**, *24*, 4144–4152. [CrossRef]
11. Liu, B.; Li, R.; Ma, X. Effect of additives on the characteristics of corn stover thermal decomposition slagging. *J. Henan Inst. Sci. Technol. (Nat. Sci. Ed.)* **2015**, *43*, 5–10+14. [CrossRef]
12. Shao, D.; Liu, W.; Luan, J.; Han, P.; Zhong, H.; Feng, H. Study on the laminar thermal decomposition characteristics of corn stover pellet fuel. *China Agric. Sci. Technol. Bull.* **2023**, *25*, 109–118. [CrossRef]
13. Al-Abedi, H.J.; Smith, J.D.; Al-Rubaye, H.; Shakor, Z.M.; Erdem, A.; Ani, P.C. Synergistic co-pyrolysis of corn stover and refuse-derived fuel with microplastics: Kinetic and thermodynamic study. *Biofuels* **2024**, *15*, 1197–1213. [CrossRef]
14. Nussbaumer, T. Thermal decomposition and Co-thermal decomposition of Biomass: Fundamentals, Technologies, and Primary Measures for Emission Reduction. *Energy Fuels* **2003**, *17*, 1510–1521. [CrossRef]
15. Huang, Z.; Wang, X.; Ren, X. Kinetic study of sesame stalk pyrolysis by thermogravimetric analysis. *Renew. Energy* **2024**, *222*, 119878. [CrossRef]
16. Zhao, S. Thermal hazards and kinetics of three organic azides. *Chem. Eng.* **2025**, *53*, 17–22.
17. Joshi, V.V.; Swaminathan, G.; Prabhakaran, S.P.S. Life cycle assessment of the co-thermal decomposition system of single-use plastic waste and lignite coal to promote circular economy. *J. Clean. Prod.* **2021**, *329*, 129579. [CrossRef]
18. Zhang, X.; Xue, W.; Zhang, X. Characterization and kinetic analysis of pyrolysis of mixed rice-corn straw. *J. Sol. Energy* **2021**, *42*, 410–414. [CrossRef]
19. Liu, L.; Liang, X.; Li, J.; Wang, D.; Luo, H.; Ren, S. Characterization and kinetic analysis of thermal decomposition of cow dung mixed with corn stover. *J. Sol. Energy* **2024**, *45*, 635–642.
20. Zhang, X.; Mutlu, Ü. TGA-FTIR Analysis of Biomass Samples Based on the Thermal Decomposition Behavior of Hemicellulose, Cellulose, and Lignin. *Energies* **2023**, *16*, 3674. [CrossRef]
21. Alsaadi, M.; Alma, M.H.; Altıkat, A.; Bilgili, M.E.; Altıkat, S. A Comprehensive Study of Biochar Yield and Quality Concerning Pyrolysis Conditions: A Multifaceted Approach. *Sustainability* **2024**, *16*, 937. [CrossRef]
22. Mishra, R.K.; Mohanty, K. Kinetic analysis and pyrolysis behaviour of waste biomass towards its bioenergy potential. *Bioresour. Technol.* **2020**, *311*, 123480. [CrossRef] [PubMed]
23. Yang, T.; Gao, Y.; Zheng, Y.; Wang, X.; He, Y. Thermal degradation kinetics of bio-based polyamide 56 fibers and their pyrolysis products. *Text. J.* **2021**, *42*, 1–7. [CrossRef]
24. Wu, W.; Mei, Y.; Zhang, L.; Liu, R.; Cai, J. Effective activation energies of lignocellulosic biomass pyrolysis. *Energy Fuels* **2014**, *28*, 3916–3923. [CrossRef]
25. Oliveira, M.; Silva, W.O.; Soutrenon, M.; Girault, H.H.; Outzourhit, A.; Alami, J.; Ghamouss, F. Biomass Screening for Syngas Production by Flash Photopyrolysis. *RSC Adv.* **2024**, *14*, D4RA01845A. [CrossRef]

26. Hu, K.; Lei, J.; Jiang, K.; Chen, Y.; Jiang, X.; Xiao, M. Thermal decomposition characteristics and kinetic features of three kinds of agricultural biomass. *J. Hubei Inst. Technol.* **2023**, *39*, 26–31. [CrossRef]
27. Liu, Y.; Yan, A.-D.; Lu, Y.-S.; Tsai, C.-H.; Tsai, W.-T. Pore and Thermochemical Properties of Biochar Materials Produced from Moso Bamboo under Different Carbonization Conditions. *Materials* **2026**, *19*, 310. [CrossRef]
28. Nanda, S.; Kantarelis, E.; Engvall, K. Effects of Porous Structure Development and Ash on the Steam Gasification Reactivity of Biochar Residues from a Commercial Gasifier at Different Temperatures. *Energies* **2020**, *13*, 5004. [CrossRef]
29. Zimmerman, A.R.; Hüffer, T.; Hofmann, T.; Kah, M. Biochar Total Surface Area and Total Pore Volume Determined by N_2 and CO_2 Physisorption Are Strongly Influenced by Degassing Temperature. *Sci. Total Environ.* **2017**, *577*, 220–229. [CrossRef]
30. Ghetti, P.; Ricca, L.; Angelini, L. Thermal analysis of biomass and corresponding pyrolysis products. *Fuel* **1996**, *75*, 565–573. [CrossRef]
31. Li, Z.; Wang, H.; Gao, Y.; Yan, L.; Wang, P.; De, X. Research on the bonding mechanism of dense molding of salix biomass fuel pellets. *J. Agric. Eng.* **2019**, *35*, 7. [CrossRef]
32. He, G. Preparation of Cellulose-Based Biomass Porous Carbon Materials and Their Electrochemical Properties. Master's Thesis, Lanzhou University of Science and Technology, Lanzhou, China, 2023; pp. 13–19.
33. Lai, J.; Luo, H.; Gu, Y.; Ren, S.; Li, H. Thermal decomposition characterization and kinetic analysis of typical biomass and its blended samples in southeast Tibet. *Plateau Agric.* **2024**, *8*, 209–216+223. [CrossRef]
34. Zhang, Y.; Shen, C.; Wang, D.; Zhang, J.; Yang, K.; Yang, H.; Liu, H.; Wen, X.; Zhang, Y.; Shao, Y.; et al. Study on Characteristics of Ash Accumulation During Co -thermal decomposition of Salix Biomass and Coal. *Energies* **2025**, *18*, 2713. [CrossRef]
35. Lin, P. *Experimental Study on the Thermal Decomposition Characteristics of Straw biomass Layer Thermal Decomposition*; Shanghai Jiaotong University: Shanghai, China, 2008; pp. 16–20.
36. Chen, T. Study on Alkali Metal Migration During Direct Thermal Decomposition Utilization of Sugarcane Bagasse. Master's Thesis, South China University of Technology, Guangzhou, China, 2014; pp. 31–36.
37. Xiao, R.; Yang, W.; Cong, X.; Dong, K.; Xu, J.; Wang, D.; Yang, X. Thermogravimetric analysis and reaction kinetics of lignocellulosic biomass pyrolysis. *Energy* **2020**, *201*, 117537. [CrossRef]
38. Vyazovkin, S.; Burnham, A.K.; Favergeon, L.; Koga, N.; Moukhina, E.; Pérez-Maqueda, L.A.; Sbirrazzuoli, N. ICTAC Kinetics Committee recommendations for analysis of multi-step kinetics. *Thermochim. Acta* **2020**, *689*, 178597. [CrossRef]
39. Kan, T.; Strezov, V.; Evans, T.J. Lignocellulosic biomass pyrolysis: A review of product properties and effects of pyrolysis parameters. *Renew. Sustain. Energy Rev.* **2016**, *57*, 1126–1140. [CrossRef]

Disclaimer/Publisher's Note: The statements, opinions and data contained in all publications are solely those of the individual author(s) and contributor(s) and not of MDPI and/or the editor(s). MDPI and/or the editor(s) disclaim responsibility for any injury to people or property resulting from any ideas, methods, instructions or products referred to in the content.